ICAS 2021 SHANGHAI
International Council of the Aeronautical Sciences
32nd Congress of the International Council of the Aeronautical Sciences
September 6-10, 2021
Pudong Shangri-La, Shanghai, China

AN OPTIMIZATION OF ANTI-ICING CHAMBER BASED ON POD AND KRIGING

Junjie.Niu[1], Weimin.Sang[1, *], Aoxiang.Qiu[1], Qilei.Guo[1] & Dong.Li[1]

[1]School of Aeronautics, Northwestern Polytechnical University, Xi'an 710072, China

Abstract

Due to the small load and the limited energy supply ice accretion on the unmanned aerial vehicles (UAVs) has limited the UAVs flight in good weather conditions. To take advantage of the energy of the UAVs as the anti/de-icing energy source may improve the UAVs application. The engine exhaust has a potential as a hot air source used for the anti-icing system. The hot air anti-icing chamber is designed and optimized. The most critical in-flight icing conditions is identified and the basic hot air anti-icing chamber is designed. The location of the piccolo tube, the angle between the jet holes are set as the design variables. The optimized latin hypercubic sampling (OLHS) is utilized and the numerical simulations are conducted. The surrogate model is built based on the proper orthogonal decomposition (POD) and Kriging interpolation. The hot air anti-icing chamber is optimized with the genetic algorithm (GA). The methodology can greatly reduce the time cost of the optimization and successfully results in optimal configurations of the anti-icing chamber.

Keywords: hot-air anti-icing; optimization; surrogated model; reduced model

1. Introduction

When the aircrafts fly through the cloud which contains the supercooled droplets, ice accretion may occur on the wing surface, the windshield and the inlet of the engines, etc. Aircraft icing has been considered as one of the most serious hazards to impact flight safety since early in the development of aviation [1]. Although many efforts have been made to solve the icing problems over the past decades, ice accretion on aircraft is still a big threat to flight safety [2]. The statistics from the National Transportation Safety Board (NTSB) shows that from June 1, 1982 to December 31, 2019, a total of 2,833 icing-related accidents occurred, including 2,362 deaths, 652 serious injuries and 922 minor injuries [3]. The anti/de-icing system of the transport aircraft has been developing for a long time and can keep the aircraft from accidents to a large extent. However, with the development of the unmanned aerial vehicles (UAVs), ice accretion poses greater challenges to the design of UAVs' anti-icing systems.

In recent years, UAVs play an important role in many fields, such as military investigations, sea ice monitoring [4-5], ship-based iceberg detection [6], search and rescue [7-8] and icing detection on wind turbines or power lines [9-10], etc. However, the icing imposes restrictions on the application of the UAVs. Literatures note that during the Kosovo War the U.S. Army's UAVs were grounded from October to April of the following year, precisely because UAVs were prone to freezing during this period [11]. UAVs have a smaller load and provide less energy for the use of anti/de-icing. Comparing with the conventional transport aircraft, there are some differences between the UAVs and the transport aircraft: the speed of the UAVs is lower, the scale of the UAVs is smaller and the energy resource used for the anti-icing is limited. However, the temperature of the engine exhaust is about 600 ℃。Therefore, the engine exhaust has a potential as a hot air resource used for the anti-icing system.

In the conventional transport aircraft the hot-air anti-icing system is mounted on the leading edge of wing [12-13]. The hot air is introduced from the compressor of the engine and ejects from the jet holes which are located on the piccolo tube. Hot air anti-icing/de-icing system utilizes the impingement jet to transfer heat from the hot air to the inner concave skin of the aircraft.

Many researches has focused on the hot air anti-icing system and impingement jet. Mattos [14], Liu [15] numerically simulated the heat transfer in the anti-icing chamber of the wing. Papadakis [16], Santos [17] experimentally and numerically studied the geometrical and operational parameters of hot air anti-icing system and the results indicated that the anti-icing performance is sensitive to the hole patterns of piccolo and the position of the piccolo related to the leading edge. Yang [18] experimentally and numerically investigated the heat transfer of impingement jet in an airfoil of NACA 0015. Wright [19] evaluated the applicability of the correlations added to the LEWICE, an icing accretion software, to simulate heat transfer of the hot air anti-icing system. Fregeau [20][21] numerically investigated the impingement jet on a 3D concave surface and studied the effects of pitch between the jet holes, the distance from the jet hole to the surface and Reynolds number on heat transfer. However, the researches mostly related to the hot air from the compressor of the engine. The temperature is relative low compared with the engine exhaust. To investigation of the engine exhaust as the hot air resource of the anti-icing system of the UAV may help improve the UAVs' application in the icing conditions.

In the present paper the exhaust gas of the engine is used as the heat resource of the hot air anti-icing system. The basic configuration of the hot air anti-icing chamber is designed. The location of the piccolo tube, the angle between the jet holes are set as the design variables. The numerical simulations are conducted with the optimized latin hypercubic sampling (OLHS). The wall temperature of each simulation is extracted. With the proper orthogonal decomposition (POD) and the Kriging interpolation, the surrogate model is established. The genetic algorithm is used to search the optimal configuration.

2. Method procedure

Figure 1 illustrates the basic flow chart of the present paper. First the most critical icing condition is identified and the basic anti-icing chamber configuration is designed. With the OLHS the three design variables are sampled. Based on the validation cases, the numerical simulations are validated and conducted. Then the wall temperature distributions of the each configurations are extracted. The POD and the Kriging interpolation are used to build the surrogate model. Finally, the optimal configuration is obtained with the GA.

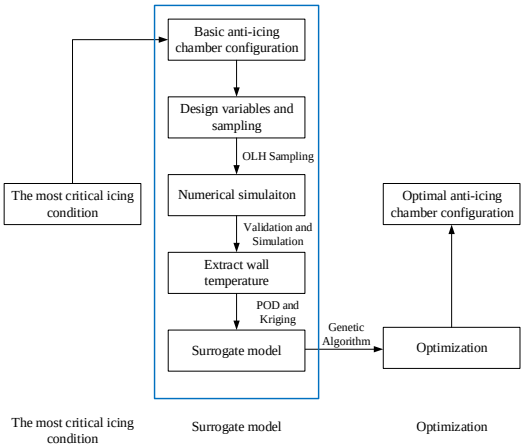

Figure 1 - Optimization methodology diagram

2.1 Optimized latin hypercubic sampling (OLHS)

Latin hypercubic sampling (LHS) is a stratified sampling method that was first proposed by McKay et al [22]. Compared with the simple random sampling method, LHS guarantees equal coverage of the cumulative probability range using non-overlapping sampling intervals and sample data in each interval. Thereby the LHS has good space-filling properties on any single dimension. However, it may have bad space-filling properties over the whole sampling space when it is randomly selected [23]. OLHS is a method that introduce an optimal criterion into the LHS process, selects the optimal Latin hypercube design on this criteria and then samples randomly based on this Latin hypercube design [24]. In the Optimal Latin hypercube technique the design space for each factor is divided uniformly (the same number of divisions, n, for all factors). These levels are randomly combined to generate a random Latin hypercube as the initial design matrix with n points (each level of a factor studies only once). An optimization process is applied to the initial random Latin Hypercube design matrix. By swapping the order of two factor levels in a column of the matrix, a new matrix is generated and the new overall spacing of points is evaluated. The goal of this optimization process is to design a matrix where the points spread as evenly as possible within the design space defined by the lower and upper level of each factor. One widely used optimality criterion is the maximin distance criterion if it maximizes the minimum inter-site distance [25]:

$$\min_{1\leqslant i,j\leqslant n, i\neq j} d(\mathbf{x}_{i,},\mathbf{x}_{j}) \tag{1}$$

where $d(\mathbf{x}_{i,},\mathbf{x}_{j})$ is the distance between two sample points $\mathbf{x}_{i}$ and $\mathbf{x}_{j}$.

$$d(\mathbf{x}_{i,},\mathbf{x}_{j}) = [\sum_{k=1}^{m} \left|\mathbf{x}_{ik} - \mathbf{x}_{jk}\right|^{t}]^{\frac{1}{t}}, \text{ t = 1 or 2} \tag{2}$$

Morris and Mitchell [26] proposed an intuitively appealing extension of the maximin distance criterion. For a given design, by sorting all the inter-sited distance $d_{i,j}$, a distance list (d_1, $d_2 \cdots d_s$) and an index list (J_1, J_2 $\cdots$ J_s) can be obtained, where d_i is distinct distance value with $d_1 < d_2 < \cdots < d_s$, J_i is the number of pairs of sites in the design separated by d_i, and s is the number of distinct distance values. A design is called a ϕ_p optimal design if it minimizes:

$$\phi_p = [\sum_{i=1}^{s} J_i d_i^{-p}]^{\frac{1}{p}} \tag{3}$$

where p is a positive integer. With a very large p the ϕ_p criterion is equivalent to the maximin distance criterion.

2.2 Proper orthogonal decomposition (POD)

Reduced-order modelling, such as POD, has already been applied in the field of CFD [27-28] and is increasing in popularity, especially in the context of CFD-based optimization. POD seeks to reconstruct an intermediate solution from a set of previously computed solutions or snapshots. Any snapshot can be decomposed as a linear combination of basis functions and associated coefficients:

$$U_j = \sum_{i=1}^{ns} \alpha_{ij} \cdot \Phi_i \tag{4}$$

The basis functions or eigenfunctions are extracted from the eigenvalue problem associated to the cross-correlation matrix related to the combined snapshots. As the vector space spanned by the

basis functions is orthonormal by definition, each coefficient is simply the dot-product of the corresponding eigenfunction with the snapshot itself. The target solution is also expressed as a linear combination of the basis functions:

$$\hat{U} = \sum_{i=1}^{nm \le ns} \hat{\alpha}_i \cdot \Phi_i \tag{5}$$

2.3 Kriging interpolation

Kriging is a method of interpolation for which the interpolated values are modeled by a Gaussian process governed by prior covariance. Under suitable assumptions on the priors, Kriging gives the best linear unbiased prediction of the intermediate values. Kriging combine a global model plus localized departures:

$$y(x) = f(x) + Z(x) \tag{6}$$

where $y(x)$ is the unknown function of interest, $f(x)$ is the known approximation function and $Z(x)$ is the realization of a stochastic process with mean zero, variance σ^2 and nonzero covariance. The $f(x)$ provides a global model of the design space. While $f(x)$ globally approximates the design space, $Z(x)$ creates localized deviations so that the Kriging model interpolates the sampled data points. The covariance matrix of $Z(x)$ is given by the following equation:

$$Cov[Z(x_i), Z(x_j)] = \sigma^2 R([R(x_i, x_j)]) \tag{7}$$

R is the correlation matrix, and $R(x_i, x_j)$ is the correlation function between any two of the sampled data points x_i and x_j. *R* is a symmetric matrix with ones along the diagonal. $R(x_i, x_j)$ is the Gaussian correlation function:

$$R(x_i, x_j) = \exp(-\sum_{k=1}^{n} \theta_k \left| x_k^i - x_k^j \right|^2) \tag{8}$$

where θ_k are the unknown correlation parameters used to fit the model and x_k^i and x_k^j are the kth components of sample points x_i and x_j. Predicted estimates, $\hat{y}(x)$, of the response $y(x)$ at untried values of **x** are given by:

$$\hat{y}(x) = \hat{\beta} + r^T R^{-1} (y - f\hat{\beta}) \tag{9}$$

where ***y*** is the column vector that contains the sample values of the response, and ***f*** is a column vector that is filled with ones when $f(x)$ is taken as a constant. r^T is the correlation vector between an untried **x** and the sampled data points {x_1, x_2 … x_{ns}}.

$$r^T(x) = [R(x, x_1), R(x, x_1) ... R(x, x_{ns})]^T \tag{10}$$

$\hat{\beta}$ is estimated using

$$\hat{\beta} = (f^T R^{-1} f)^{-1} f^T R^{-1} y \tag{11}$$

The estimate of the variance $\hat{\sigma}^2$ is estimated by

$$\hat{\sigma}^2 = [(y - f\hat{\beta})R^{-1}(y - f\hat{\beta})] / n_s \tag{12}$$

where $f(x)$ is assumed to be the constant $\hat{\beta}$. The maximum likelihood estimates for the θ_k used to fit a Kriging model are obtained by solving following equation:

$$\max \Phi(\theta_k) = -\left[n_s \ln(\hat{\sigma}^2) + \ln|\mathbf{R}| \right] / 2 \tag{13}$$

where both $\hat{\sigma}^2$ and $|\mathbf{R}|$ are functions of θ_k. While any value for the θ_k creates an interpolative kriging model, the best kriging model is found by solving the k-dimensional unconstrained nonlinear optimization problem given by equation (13).

2.4 Genetic algorithms (GA)

In computer science and operations research, a genetic algorithm (GA) is a method inspired by the process of natural selection that belongs to the larger class of evolutionary algorithms (EA). Genetic algorithms are commonly used to generate high-quality solutions to optimization and search problems by relying on biologically inspired operators such as mutation, crossover and selection [29]. In a genetic algorithm, a population of candidate solutions (called individuals, creatures, or phenotypes) to an optimization problem is evolved toward better solutions. Each candidate solution has a set of properties which can be mutated and altered. The evolution usually starts from a population of randomly generated individuals, and is an iterative process, with the population in each iteration called a generation. In each generation, the fitness of every individual in the population is evaluated; the fitness is usually the value of the objective function in the optimization problem being solved. The more fit individuals are stochastically selected from the current population, and each individual's genome is modified to form a new generation. The new generation of candidate solutions is then used in the next iteration of the algorithm. The algorithm terminates when either a maximum number of generations has been produced, or a satisfactory fitness level has been reached for the population. The present paper uses the GA in the matlab optimization toolbox to find the optimal configuration.

In the present paper the GA module was configured in the following manner. The reproduction method relies on a single point cross-over fraction of 80% (thus a 20% mutation rate) and an elite count of two. The population size is 30 for the three design variables. No subpopulations were used and the number of generations was set to 50. Thus a GA population of 30 individuals for 50 generations leads to 1500 evaluations and 1500 associated computations. The Papadakis [30] indicates that to achieve an full evaporation the wall temperature needs to exceed 322.15K。 Therefore，the objective function would be to maximize the average value of the wall temperature.

3. Numerical simulation

3.1 Governing equations

The governing equations include the mass, momentum and energy conservation equations, as shown as follows:

$$\frac{\partial \rho}{\partial t} + \frac{\partial （\rho \mathbf{u}_i）}{\partial \mathbf{x}_i} = 0 \tag{14}$$

where ρ is the air density, $\mathbf{u}_i$ is the air speed;

$$\frac{\partial \rho}{\partial t}+\frac{\partial(\rho \mathbf{u}_i \mathbf{u}_j)}{\partial \mathbf{x}_j}=-\frac{\partial P}{\partial \mathbf{x}_i}+\frac{\partial}{\partial \mathbf{x}_j}(\mu(2\mathbf{S}_{ij})-\rho\overline{\mathbf{u}_i^{'}\mathbf{u}_j^{'}}) \tag{15}$$

where *P* is the pressure, $\mathbf{S}_{ij}$ is the stress tensor and $\overline{\mathbf{u}_i^{'}\mathbf{u}_j^{'}}$ is the turbulent stress tensor;

$$\frac{\partial(\rho c_p T)}{\partial t}+\frac{\partial(\rho c_p \mathbf{u}_i T)}{\partial \mathbf{x}_j}=\frac{\partial}{\partial \mathbf{x}_j}(\kappa\frac{\partial T}{\partial \mathbf{x}_i}-\rho c_p\overline{\mathbf{u}_i^{'}T^{'}}) \tag{16}$$

where $\overline{\mathbf{u}_i^{'}T^{'}}$ is the turbulent heat flux. The SST k-ω turbulence model is used to simulate the flow, which has been proved that the turbulence model can give a good result of the heat transfer of the impingement jets [31-33]. The turbulent kinetic energy k and the turbulent dissipation rate ω can be obtained by the following equations:

$$\frac{\partial}{\partial t}(\rho k)+\frac{\partial}{\partial \mathbf{x}_i}(\rho k \mathbf{u}_i)=\frac{\partial}{\partial \mathbf{x}_j}(\Gamma_k\frac{\partial k}{\partial \mathbf{x}_j})+G_k-Y_k \tag{17}$$

$$\frac{\partial}{\partial t}(\rho \omega)+\frac{\partial}{\partial \mathbf{x}_i}(\rho \omega \mathbf{u}_i)=\frac{\partial}{\partial \mathbf{x}_j}(\Gamma_\omega\frac{\partial \omega}{\partial \mathbf{x}_j})+G_\omega-Y_\omega \tag{18}$$

where G_k is the generation term of turbulent kinetic energy due to the average velocity gradient, G_ω is the generation term of dissipation rate, Γ_k and Γ_ω are the effective diffusion of k and ω respectively and Y_k and Y_ω are the dissipation due to turbulence, respectively. The details of the SST k-ω turbulence model can refer to Menter [34].

In this paper, the SIMPLE algorithm is used to solve the basic equations. The pressure, momentum, turbulent kinetic energy and energy terms are discretized in a second-order manner. The pressure and momentum relaxation is 0.4 and the convergence accuracy is set as 1e-5.

3.2 Validation

The HAARP (Hot Air Anti-icing Research Project) is dedicated to developing low-cost experimental methods for the evaluation of the hot air anti-icing systems, conducting the parameter studies of the hot air anti-icing systems and using commercial software to simulate the anti-icing system and validate experimental data to determine the usability of the commercial software in the design and the performance analysis of the hot air anti-icing systems [35-36]. The HAARP project has obtained rich achievements and the experimental conditions and results in the literature are relatively complete. Therefore, this paper adopts parts of the HAARP operating conditions for validation.

The model of the HAARP project includes two parts: internal flow part and external flow part. The external flow part includes the airfoil and the wind tunnel. The internal flow part contains an anti-icing chamber with a piccolo tube. The model of the HAARP project is shown in the Figure 2 to Figure 5. Figure 2 is a schematic diagram of the external flow part and the grid; Figure 3 is a schematic diagram of the anti-icing chamber at the leading edge of the airfoil, in which two circular jet holes are arranged in the middle of the piccolo tube and the other two semicircular jet holes are arranged in the middle of the two ends of the piccolo tube. Figure 3 also shows three sections in the anti-icing chamber, which are section AA, BB, and CC, where AA section is the section in the chord direction at the center of the two jet holes which are located in the middle of the piccolo tube and BB section is the section in the chord direction at the one end of the piccolo tube, the CC section is the spanwise section at the center of the two semicircular jet hole at both ends of the piccolo tube. Figure 4 and

Figure 5 are schematic diagrams of the grids at the AA and BB sections respectively and the grids in the jet impingement direction are refined.

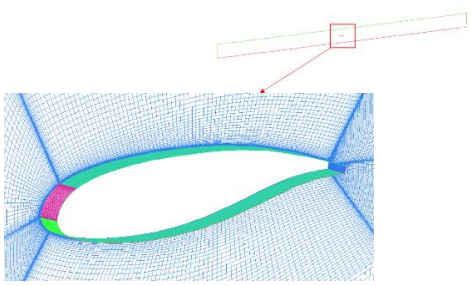

Figure 2 - Sketch of model and grid of external flow part of the HAARP project

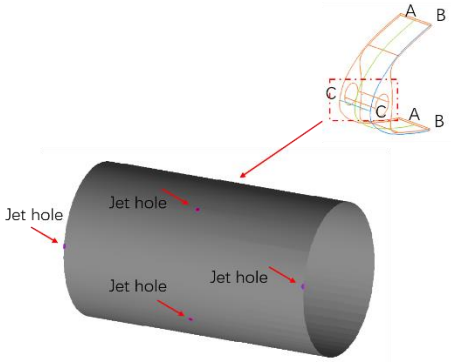

Figure 3 - Anti-icing chamber model and partial enlargement of the HAARP project

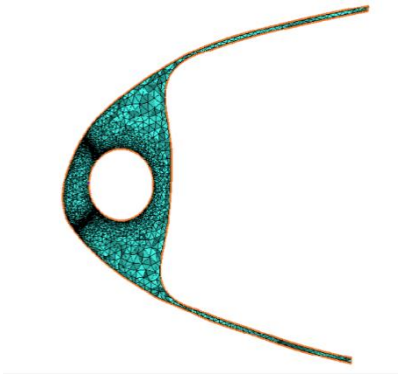

Figure 4 - Grid sketch of the AA section

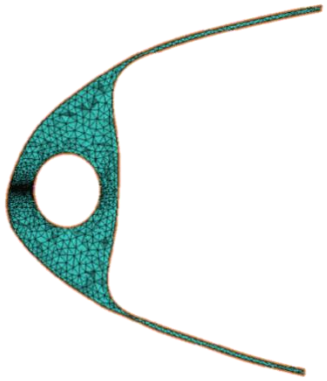

Figure 5 - Grid sketch of the BB section

The dry air condition of Run26 and the wet air condition of Run39 are chosen as the validation cases. The conditions of the two cases are nearly the same except that the Run39 is sprayed with the supercooled water droplets. The conditions of the Run26 and the Run39 are shown in Table 1 and the icing conditions of the Run39 are shown in Table 2.

Table 1 - Boundary conditions of the validation cases

	External	Internal
Inlet total pressure/Pa	99112	166508
Inlet total temperature/K	268.15	463.15
Outlet static pressure/Pa	96526	111350
Turbulence intensity/%	1	4
Hydraulic diameter/m	2.195	0.03175
Angel of attack/°	3	

Table 2 - Icing conditions of Run39

Parameters	Values
T/K	266.45
MVD/μm	29
LWC/(g/m³)	0.87

The internal flow and external flow are calculated separately and the wall temperature distribution is obtained through internal and external coupling. The simulation is validated by comparing the temperature distribution of BB section with the experimental data in the literature The wall

temperature distributions of the BB section are shown in Figure 6 and Figure 7. It can be seen that the highest temperature is at the stagnation point where the jet impinges directly and the temperature gradually decreases along the surface distance from the leading point. The Figure 6 and the Figure 7 indicate that the numerical simulation results are in good agreement with the experimental results.

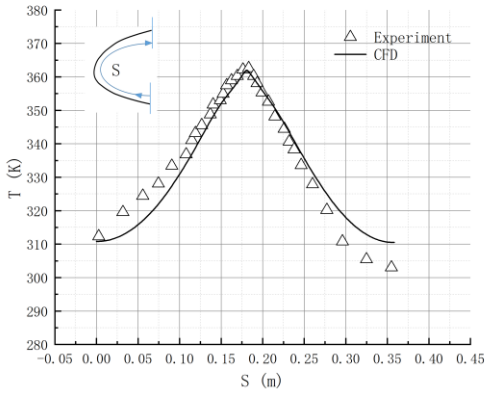

Figure 6 - Temperature distribution comparison of Run26

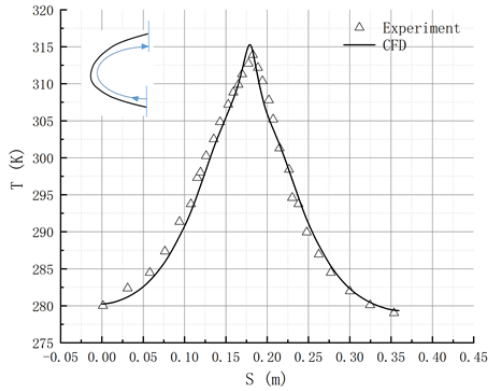

Figure 7 - Temperature distribution comparison of Run39

3.3 Model and sampling

The heat transfer in the anti-icing chamber depends heavily on the distance between the jet hole and the leading edge and the angles between the jet holes. Therefore the ratio s/d and the angles are set as design variables. The s is the distance between the jet hole and the leading edge and the d is the diameter of the jet hole. The sketch diagram of the anti-icing chamber is showed in the Figure 8. Figure 8 illustrates the basic configuration of hot air anti-icing chamber. The piccolo tube is located in the center of the chamber. And three rows jet holes are set on the piccolo tube. The two semicircular jet holes which are in the middle row are directly facing the leading edge of the wing. The area near the leading edge usually has a large droplets collection. The distance between the hole and the leading edge is s. The other rows of the jet holes are located in the two sides of the middle row. The angles between holes are θ_1 and θ_2 . In the present paper the two angles and the distance ratio s/d are set as design variables. The diameter of the piccolo tube and the jet holes are fixed. The distance ratio s/d s is in the range of 3-15, where the d is the diameter of the jet holes. The angle range is 0-45° . The design variables are illustrated in the Figure 9.

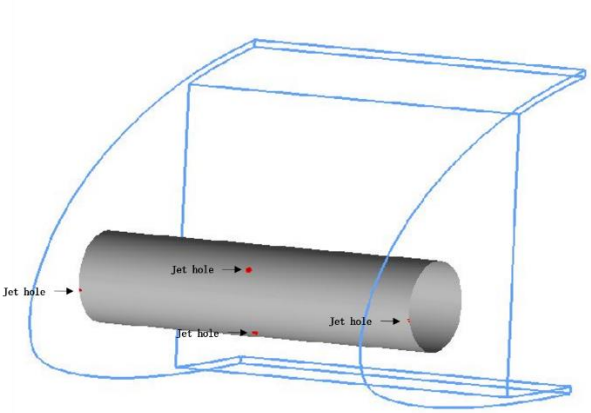

Figure 8 - The sketch diagram of the anti-icing chamber

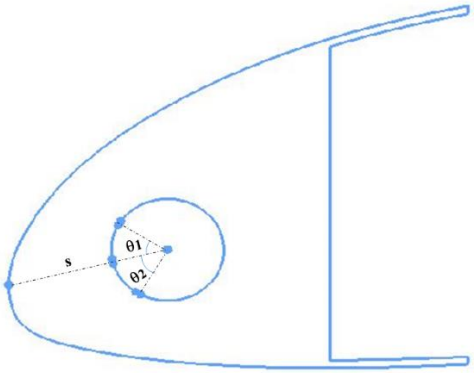

Figure 9 - The sketch diagram of the design variables

With the OLHS, 30 configurations are numerically simulated. The 30 configurations is showed in the Table 3.

Table 3 - The 30 configurations of the anti-icing chamber

No.	1	2	3	4	5	6	7	8	9	10
θ_1	41.9	6.21	34.14	20.17	43.45	9.31	35.69	45	10.86	38.79
θ_2	6.21	12.41	43.45	41.9	32.59	3.1	4.66	21.72	45	13.97
s/d	10.86	12.93	7.97	11.69	5.48	8.38	6.72	8.79	5.07	3.41
No.	11	12	13	14	15	16	17	18	19	20
θ_1	3.1	18.62	4.66	24.83	32.59	40.34	26.38	21.72	31.03	15.52
θ_2	38.79	34.14	9.31	10.86	1.55	20.17	31.03	7.76	23.28	24.83
s/d	10.03	7.55	4.24	9.62	14.17	13.34	15	4.66	6.31	3
No.	21	22	23	24	25	26	27	28	29	30
θ_1	12.41	0	23.28	29.48	37.24	7.76	17.07	1.55	13.97	27.93
θ_2	26.38	17.07	15.52	27.93	40.34	35.69	0	29.48	18.62	37.24
s/d	11.28	9.21	13.76	10.45	12.52	14.59	12.1	5.9	7.14	3.83

4. Result and discussion

The ice accretion on the UAVs is related to the flight conditions (angle of attack (AOA), velocity, height) and the icing conditions (mean volume diameter (MVD), liquid water content (LWC) and temperature (T)). Besides, MVD, LWC and temperature are related to the height and the droplets impingement property is related to the AOA and velocity. Zhao [11] noted that the holding condition is considered as one of the most critical icing condition for the maximum total catch rate. Therefore, the holding condition is set as the design point in the present paper. The Table 4 illustrates the icing and flight conditions in the holding condition.

Table 4 - Icing and flight conditions

LWC(g/m³)	MVD(μm)	T(K)	Height(m)	V(m/s)	AOA(°)
0.429	20	263.35	3000	100	0

As the same in the validation cases, the external and the internal parts are simulated separately and the wall temperature is obtained with coupling. The temperature contours of case 20, 13, 28, 29, 22, 11 and 27 and case 17 are shown in the Figure 10, corresponding to s/d of 3, 4.24, 5.9, 7.14, 9.21, 10.03, 12 and 15, respectively. It can be seen that with the increase of s/d, the temperature of the area directly opposite the two semicircular jet holes on the leading edge of the wing first increases and then decreases. This is because the heat transfer ability of the impingement jet has a strong relationship with the distance between the jet hole and the impinging wall. After the impinging jet flows out of the jet hole, the jet and the surrounding fluid are continuously mixed. The core of the jet, which is also called potential core area, decreases with the increase of the jet distance. At the same time, the overall turbulence of the jet increases gradually. The potential core area disappears when s/d is about 6 and the overall turbulence intensity increases to the maximum which leads to a strong heat transfer between the hot air and the wall. After that, with the increase of jet distance and the mixing of surrounding fluid the turbulence intensity of the jet decreases gradually and the heat transfer ability also decreases.

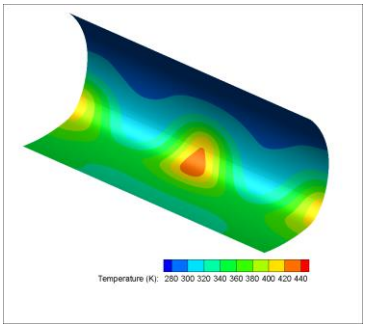

a) Case20

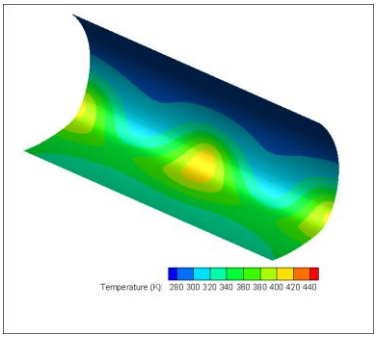

b) Case 13

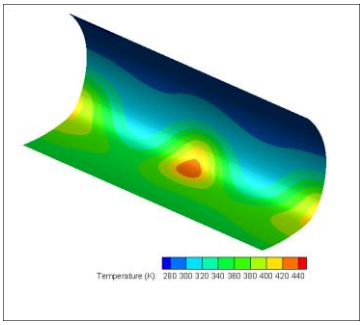

c) Case28

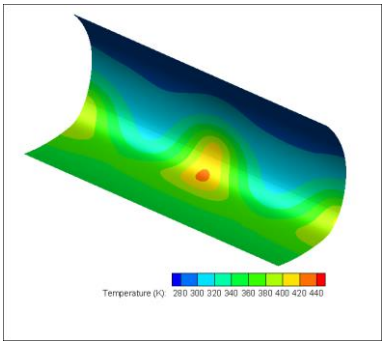

d) Case29

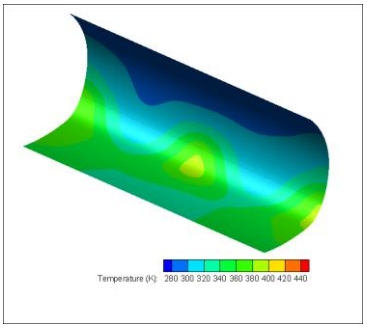

e) Case22

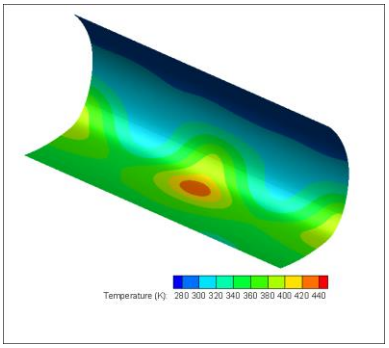

f) Case11

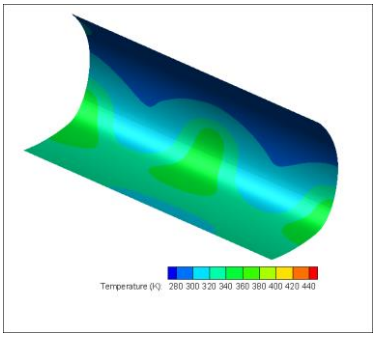

g) Case27

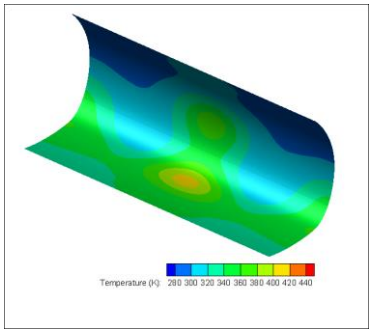

h) Case17

Figure 10 - The temperature contour with different configurations

The wall temperature distributions of the 30 configurations are extracted to build the surrogated model. In the process of the POD, the basis functions are extracted from the eigenvalue problem associated to the cross-correlation matrix related to the combined snapshots. Solving the eigenvalue problem provides an eigenvalue-eigenvector pair for each mode, sorted form the highest to the lowest in terms of energy content, the principal features being contained into the most energetic modes. Thus, a few of modes (corresponding to a cumulative energy content of 99%) would usually suffice to obtain the target computed solution, decreasing to some extent the computational cost.

Figure 11 illustrates the maximum error between POD prediction and the CFD results of the 30 configuration. It can be seen that with the increase of eigenvalue, the maximum error decreases rapidly to a certain level. With the help of the first fifteen eigenvalues the maximum error can decrease to 5K. As a result, the present paper chooses the first fifteen eigenvalues to build the surrogated model.

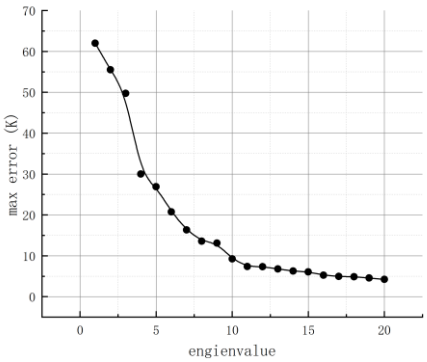

Figure 11 - The max error with cumulative eigenvalues

The optimum anti-icing chamber configuration is obtained with the GA. The optimum s/d is 4.5 and the optimum θ_1 and θ_2 are 38° and 37.92° , respectively. The average wall temperature is 333.9K. The whole process of the surrogated model optimization is about 5 hours, which is much less than the time in the numerical simulation. Figure 12 illustrate the wall temperature contour and the Figure 13 illustrates the ice accretion of the wing in the holding condition in 5min. It can be seen that there is no ice accretion on the surface which indicates that the anti-icing system is effective and the exhaust gas of the UAVs can be used as the hot air resource for the anti-icing system.

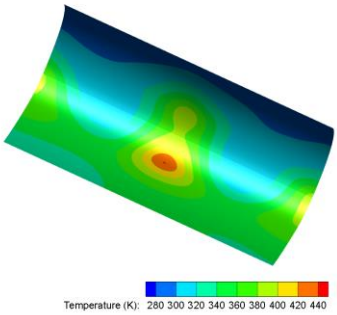

Figure 12 - Wall temperature contour of the optimum configuration

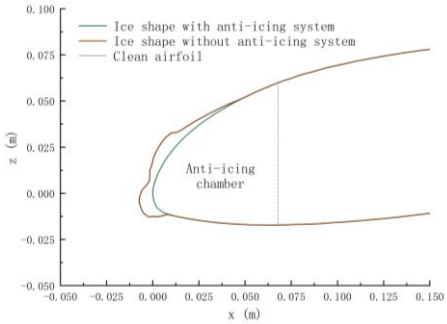

Figure 13 - Ice accretion on the wing comparison with and without hot air anti-icing

5. Conclusion

The application of the UAVs are becoming more and more extensive in many fields. However the ice accretion poses a serious threat to the safe flight of the UAVs. To utilize the engine exhaust gas as the hot air resource for the anti-icing system provides a possible method for the anti-icing system of the UAVs. With the help of OLHS, numerical simulation, POD and Kriging interpolation the surrogated model of the hot air anti-icing chamber is built. The optimum configuration of anti-icing chamber is obtained with the GA. The method can reduce the time cost of the optimization greatly.

In the present paper the objective function of the GA is chosen to maximize the average wall temperature. However, the droplets collection decreases with the distance from the stagnation. It means that the heat requirement is different along the surface of the wing. The objective function of the GA needs optimization further. This work will be added in the future work.

6. Acknowledgment

This work has benefited greatly from the support of the National Key Project of China under grant GJXM92579 and the Open Fund of Key Laboratory of Icing and Anti/De-icing of China under grant IADL20200101.

7. Contact Author Email Address

Weimin. Sang, email: sangweimin@nwpu.edu.cn

Junjie. Niu, email: niu_junjie@outlook.com

8. Copyright Statement

References

[1] Smith W L. Weather problems peculiar to the New York-Chicago airway. Monthly Weather Review, Vol. 57, No. 12, pp 503-506, 1929.

[2] Potapczuk M G. Aircraft icing research at NASA Glenn research center. Journal of Aerospace Engineering, Vol. 26, No. 2, pp 260-276.2013.

[3] https://www.ntsb.gov/Pages/default.aspx

[4] Wang M, Su J, Li T, et al. Determination of Arctic melt pond fraction and sea ice roughness from Unmanned Aerial Vehicle (UAV) imagery. Advances in Polar Sciences, Vol. 29, No.3, pp 181-189, 2018.

[5] Leira F S, Johansen T A, Fossen T I. A UAV ice tracking framework for autonomous sea ice management. 2017 International Conference on Unmanned Aircraft Systems (ICUAS). pp 581-590, 2017.

[6] Langeveld S M. Unmanned aerial vehicle mission planning for combined iceberg detection and tracking missions. NTNU, 2017.

[7] Scherer J, Yahyanejad S, Hayat S, et al. An autonomous multi-UAV system for search and rescue. Proceedings of the First Workshop on Micro Aerial Vehicle Networks, Systems, and Applications for Civilian Use. pp 33-38, 2015.

[8] Naidoo Y, Stopforth R, Bright G. Development of an UAV for search & rescue applications. Africon. IEEE, pp 1-6, 2011.

[9] Li Z, Liu Y, Hayward R, et al. Knowledge-based power line detection for UAV surveillance and inspection systems. 2008 23rd International Conference Image and Vision Computing New Zealand. IEEE, pp 1-6, 2008.

[10] Bhola R, Krishna N H, Ramesh K N, et al. Detection of the power lines in UAV remote sensed images using spectral-spatial methods. Journal of environmental management, Vol. 206, pp 1233-1242, 2018.

[11] Zhao. K. L. Icing calculation, wing tunnel experiment and flight test for large civil aircraft . Nanjing University of Aeronautics and Astronautics, 2017.

[12] Planquart P, Borre G. V, Buchlin J. M, Experimental and numerical optimization of a wing leading edge hot air anti-icing system. 43rd AIAA Aerospace Sciences Meeting and Exhibit. pp 1277, 2005.

[13] Saeed F, Numerical simulation of surface heat transfer from an array of hot-air jets, Journal of Aircraft. Vol. 45, No.2, pp 700-714, 2008.

[14] Mattos, Bento, Oliveira, Guilherme. Three-dimensional thermal coupled analysis of a wing slice slat with a piccolo tube. 18th Applied Aerodynamics Conference, pp 3921, 2000.

[15] Liu H T, Hua J, et al. Three-dimensional integrated thermodynamic simulation for wing anti-icing system. Journal of Aircraft, Vol.41, No.6 pp1291-1297, 2004.

[16] Papadakis M, Wong S H, Yeong H W, et al. Experimental investigation of a bleed air ice protection system. SAE Transactions, pp 643-663, 2007.

[17] Santos L, Domingos R, Maria R, et al. Sensitivity analysis of a bleed air anti-ice thermal model to geometrical and operational parameters. 46th AIAA Aerospace Sciences Meeting and Exhibit. pp 445 2008.

[18] Yang B, Chang S, Wu H. Experimental and numerical investigation of heat transfer in an array of impingment jet on a concave surface . Applied Thermal Engiveering. Vol. 127, pp 473-483, 2017.

[19] Wright B W. An evaluation of jet impingement heat transfer correlations for piccolo tube application. 42nd AIAA aerospace sciences meeting and exhibit, Reno Nevada, pp 62, 2004.

[20] Fregeau M, Paraschivoiu I, Saeed F. Numerical heat transfer correlation for array of hot-air jets impinging on 3dimensional concave surface. Journal of Aircraft, Vol. 42, No. 3, pp 665-670, 2005.

[21] Fregeau. M, Gabr. M, Paraschivoiu. I. Simulation of heat transfer from hot-air jets impinging a three-dimensional concave surface. Journal of Aircraft, Vol. 46, No.2, pp 721-726, 2009.

[22] Mckay M D, Conover R J B J. A comparison of three methods for selecting values of input variables in the analysis of output from a computer code. Technometrics, Vol. 21, No. 2, pp 239-245, 1979.

[23] Jourdan A, Franco J. Optimal Latin hypercube designs fortheKullback–Leibler criterion. Asta Advances in Statistical Analysis, Vol. 94, No. 4, pp 341-351, 2010.

[24] Ye K Q, Li W, Sudjianto A. Algorithmic construction of optimal symmetric Latin hypercube designs - ScienceDirect. Journal of Statistical Planning & Inference, Vol. 90, No. 1, pp 145-159, 2000.

[25] Johnson, M., L. Moore, and D. Ylvisaker, Minimax and maximin distance designs. Journal of Statistical Planning and Inference, Vol. 26, pp. 131–148, 1990.

[26] Morris, M. D., and T. J. Mitchell. Exploratory designs for computational experiments, Journal of Statistical Planning and Inference, Vol. 43, pp. 381–402, 1995

[27] Shen X B, Yu J and Lin G P, et al. Fast prediction of ice shape based on proper orthogonal decomposition method. Journal of Aerospace Power. Vol.28, No.4, pp. 807-812, 2013.

[28] Ostrowski Z, Bialecki R A. Estimation of constant thermal conductivity by use of proper orthogonal decomposition. Computational Mechanics, Vol.37, No.1, pp.52-59, 2005.

[29]Mitchell M. An Introduction to Genetic Algorithms. MIT Press, Cambridge. DBLP, 1998.

[30]Papadakis M, Wong S H, Yeong H W, et al. Parametric investigation of a bleed air ice protection system. AIAA Aerospace Sciences Meeting & exhibit. pp 1013, 2007.

[31]Uddin N, Wigand B. LES simulations of an impinging jet: On the origin of the second peak in the Nusselt number distribution. International Journal of Heat and Mass Transfer, Vol. 57, No. 1, pp 356-368, 2013.

[32]Guo Z Q, Zheng M. Dong W, et al. Influence of surface convex on heat transfer enhancement of wing hot air anti-icing system. Journal of aeronautics, Vol. 38, No. 2, pp 81-90, 2017.

[33]Afroz F, Sharif M A R. Numerical investigation of the heat transfer due to coaxial swirling turbulent jet impingement on heated flat surfaces. 8th BSME Internal Conference on thermal Engineering. Vol. 2121, No.1, pp 030008, 2019

[34]Menter, F. R. Two-equation eddy-viscosity turbulence models for engineering applications. AIAA Journal, Vol. 32, No. 8, pp 1598-1605, 1994.

[35]Zamora A O. Numerical investigation of a wing hot air ice protection system. M. Sc. Thesis, Department of Aerospace Engineering, Wichita State University, Wichita, KS, 2007.

[36]Papadakis M, Wong S H, Yeong H W, et al. Icing tunnel experiments with a hot air anti-icing system. AIAA Aerospace Sciences Meeting & Exhit. pp 444,2008.